

Research Article

Preliminary Study on High-Energy and Low-Energy Microfracture Event Evolution Characteristics in the Development Process of Rock Failure

Guofeng Yu,^{1,2} Guanwen Cheng ,³ Lianchong Li,³ Chunan Tang,⁴ Bo Ren,² and Yunchun Han³

¹School of Energy and Safety, Anhui University of Science and Technology, Huainan 232001, China

²State Key Laboratory of Deep Coal Mining and Environmental Protection, Huainan Mining (Group) Co., Ltd., Huainan 232001, China

³Center for Rock Instability and Seismicity Research, Northeastern University, Shenyang 110819, China

⁴State Key Laboratory of Coastal and Offshore Engineering, Dalian University of Technology, Dalian 116023, China

Correspondence should be addressed to Guanwen Cheng; chengguanwen@mail.neu.edu.cn

Received 20 May 2020; Revised 6 July 2020; Accepted 21 August 2020; Published 14 September 2020

Academic Editor: Jingmin Xu

Copyright © 2020 Guofeng Yu et al. This is an open access article distributed under the Creative Commons Attribution License, which permits unrestricted use, distribution, and reproduction in any medium, provided the original work is properly cited.

The evolution characteristics of high-energy and low-energy microfracture events play an important role in the brittle failure mechanism of rock and reasonable microseismic (MS) monitoring and acoustic emission (AE) monitoring. The bimodal distribution (BMD) model is commonly used to observe the evolution characteristics of high-energy and low-energy MS events; however, its precise mechanism remains unclear. The evolution characteristics of high-energy and low-energy microfracture events are assessed in this study based on a BMD model. MS monitoring results from the No. 22517 working face of the Dongjiahe Coal Mine are studied, and AE monitoring results of a biaxial compression experiment of a granite specimen are analyzed. High-energy MS events in the No. 22517 working face are found to be generated by an increase in the failure scale of the overlying rock mass upon exiting the insufficient mining stage and entering the sufficient mining stage. The change characteristics of the high-energy AE hits are positively correlated with crack evolution characteristics in the granite specimen and negatively correlated with changes in the Gutenberg-Richter b value. A precise high-energy and low-energy AE hit evolution mechanism is analyzed based on the microscopic structure of the granite specimen. Similarities and differences between high-energy MS events and low-energy AE hits are determined based on these results. Both are found to have bimodal characteristics; an increase in the failure scale is identified as the root cause of the high-energy component. The bimodal distribution of AE hits is far less obvious than that of MS events.

1. Introduction

In a study on the recurrence of large seismic events in Polish mines, Gibowicz and Kijko [1] found that the pattern of empirical distributions of the largest seismic events is more complex than expected based on the most general theoretical considerations (e.g., Gumbel distributions) [2]. The observed distributions possess bimodal distribution (BMD) characteristics, as shown in Figure 1 BMD has also been observed in the underground coal mines of Upper Silesia, Poland, at the

Doubrava coal mine of the Ostrava-Karvina Coal Field, Czechoslovakia, and in the copper ore mines of Lubin Copper Basin, Poland [1]. The seismicity associated with the eruption of Mount St. Helens, Washington, in May 1980 obeyed the BMD as confirmed by the distribution of characteristic periods in the maximum amplitude signals and by the frequency-magnitude relations [3]. Another striking example of BMD was found in New Madrid, Missouri, and interpreted as a result of the superposition of two distinct seismogenic source types observed in the area [4].

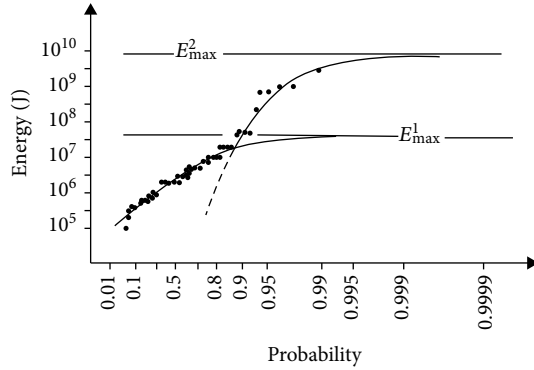


FIGURE 1: Probability distribution of the monthly occurrence of maximum magnitude tremors at the Lubin copper mine, Poland, for the period 1972-1980 [6].

The BMD results from the mixing of random variables generated by two different phenomena. The first phenomenon is responsible for the low-energy component and the second one for the high-energy component of the distribution. At present, the BMD is considered an important method for observing the evolution characteristics of high-energy and low-energy microseismic (MS) events.

Despite many valuable contributions to the literature, the precise mechanism of the BMD is not yet known. The traditional view is that the BMD obeys at least three statistical distributions. The first was proposed by Stankiewicz [5], who assumed that at any moment, the state of the rock mass can be described by a stress that increases linearly in time in the absence of a seismic event and drops to a certain value from the interval if an event occurs. The other two statistical distributions were proposed by Gibowicz and Kijko [1]. Under the second statistical distribution, high- and low-energy seismicity are independent of each other. Under the third statistical distribution, the high-energy seismicity is dependent on the low-energy seismicity. Monitoring data can be well fitted to these three statistical distributions, but none fully characterizes the BMD mechanism.

There are two hypotheses as to the nature of the two sets of events discussed above [6]. The first states that BMD is a result of the inhomogeneous and discontinuous structure of the rock mass. The second states that the low-energy component of the distribution is a result of mine-induced stress release, while the high-energy component is a result of the interaction between mine-induced and residual tectonic stresses in the area. The first hypothesis is acceptable in certain mining districts and the second hypothesis in others, where geologic factors play by far the most important role in the generation of seismic events in mines.

The early warning mechanism of mine disaster is closely related to the rock and fissures, and the evolution characteristics of high-energy and low-energy microfracture events monitored by microseismic early warning are of great significance to the failure mechanism of rocks [7, 8]. Many previous researchers have conducted laboratory and in situ research by acoustic emission (AE) and MS monitoring technologies. In the field of MS monitoring, Xiao et al. [9], Feng et al. [10], Xu et al. [11], and Yu et al. [12, 13] studied the rela-

tionships between monitored MS activities and rockburst events in tunnels; rockburst events can be predicted by capturing MS events produced during the excavation of a rock. Zhang et al. (2017), Wang et al. [14], and Cheng et al. [15] studied the relationship between the MS event distribution and strata movement caused by underground mining. Cao et al. [16, 17] and Li et al. [18] investigated the relationship between MS activities and rockburst events to predict possible rockburst locations in coal mines. Lu et al. [19] and Li et al. [20] studied the relationship between the distribution of MS events and coal-gas outburst in a coal mine. Li et al. [7], Zhang et al. [21], and Wang et al. [14] studied the relationship between MS monitoring results and water inrush. They found that fractured zones in rock masses, which may form water inrush channels, can be determined according to the spatial distribution of MS events.

Xu et al. [22], Dai et al. [23], and Salvoni et al. [24] carried out MS monitoring during the excavation of slopes and to find that ground deformation and MS data reflect rock damage at various depths as well as mechanisms of rock mass instability. Previous studies have also shown that the occurrence of MS events is closely related to failure rock mass and related disasters. AE evolution characteristics have been analyzed based on six main factors: number and energy [25–27], frequency [28, 29], spatial location [30–32], spatial correlation length [33], fractal dimension [34, 35], and moment tensor [36]. Dixon et al. [37, 38] and Smith [39, 40] used AE monitoring for slope deformation and stability predictions. These previous studies provide a workable basis for studying the evolution characteristics of high-energy and low-energy microfracture events related to the BMD mechanism.

Inspired by previous research results, MS monitoring was carried out in No. 22517 working face in the Dongjiahe Coal Mine in this study. A biaxial compression experiment was also performed with a granite specimen in the laboratory. The MS monitoring and experimental results were analyzed to determine the evolution characteristics of high- and low-energy microfracture events. The relationship between the evolution characteristics and various failure scales were observed to determine the BMD mechanism. Finally, the similarities and differences between high-energy MS event and low-energy AE hit evolution characteristics were determined as discussed in detail below.

2. Evolution Characteristics of High-Energy and Low-Energy AE Hits

2.1. Experimental System. The biaxial compression experimental system used in this study is composed of a rock mechanic testing system, an AE monitoring system, and an observation system (Figure 2(a)). The experiment was conducted on a servocontrolled rock testing machine (RLW-3000). The loading was applied in both horizontal and vertical directions. The maximum axial loading was 3000 kN, the maximum horizontal loading was 1000 kN, and the measurement error of loading force was less than 1%.

The AE activities were recorded on an eight-channel PCI-2 AE monitoring system (Physical Acoustic Corporation). The bandwidth of the AE acquisition card is 3 kHz-

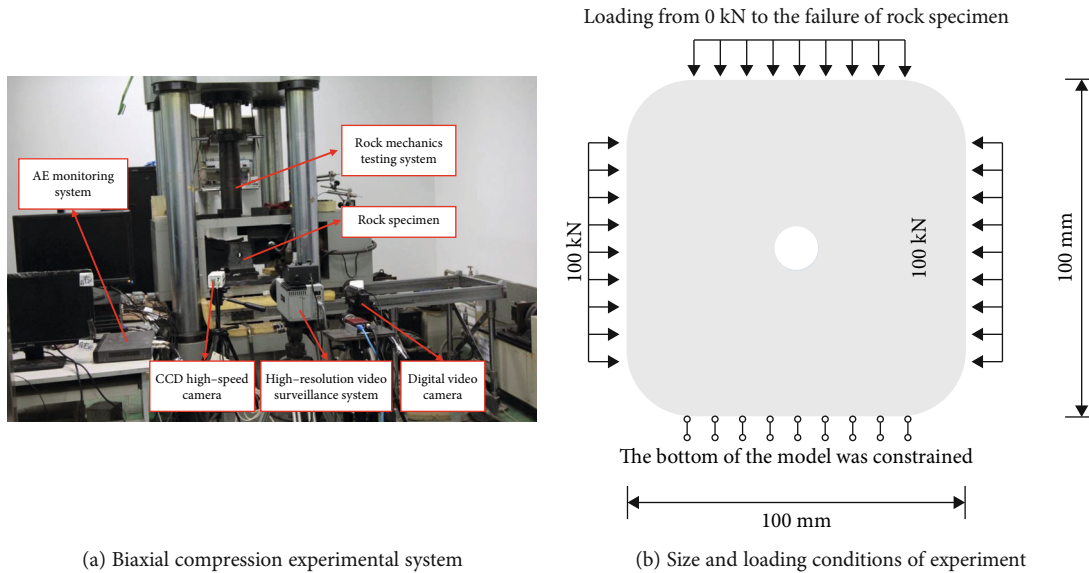


FIGURE 2: Biaxial compression experiment using AE monitoring.

3 MHz. An R6a sensor was used which has working temperature from -65-175 degrees Celsius, size of 19*22 mm, frequency range of 35-100 kHz, and center frequency of 60 kHz. The magnification is adjustable to 20, 40, and 60 dB over three gears. The observation system consists of a CCD high-speed camera, a high-resolution video surveillance system, and a digital video camera which can obtain images during crack development and rock failure.

The test granite specimen in this experiment was a cube with side length of 100 mm and a 15 mm-diameter circular opening in the middle (Figure 2(b)). Before AE monitoring began, the horizontal and vertical loads were gradually loaded to 10 kN by stress loading. The vertical load was stopped as the horizontal load continued to 100 kN and was held unchanged by the servocontrol system. AE sensors with 40 dB threshold and 1 MHz sampling frequency were then arranged on the specimens for AE monitoring. The loading applied at the upper side increased from 10 kN until failure of the granite specimen. The bottom end was prevented from displacement in the vertical direction. The sampling frequency of the high-speed video was 100 frames per second.

2.2. Experimental Results

2.2.1. Axial Load-Displacement Curve and Fracture Evolution Process. The axial load-displacement curve was determined as shown in Figure 3. Based on the biaxial compression load-displacement curve, three feature points (A, B, and C) were identified. Point A is the critical point from the compaction stage to elastic deformation, point B is the critical point from elastic deformation to inelastic deformation, and point C is the peak stress of the load-displacement curve. At Point A, the axial loading force of the granite specimen was equal to the lateral loading force. Li et al. [18] showed that when the stress increases to 78.2% of the peak loading value, critical cracks initiate in the tensile stress concentration zones under uniaxial loading conditions; similar results were also reached

by Zhong et al. [41]. Based on previous research, the axial loading force at Point B was determined to be 80% of the peak stress under biaxial loading.

As shown in Figure 3, the axial force was 100.14 kN at Point A, 677.29 kN at Point B, and 846.59 kN at Point C. The ratio of the lateral loading force to the axial loading force was defined as the lateral pressure coefficient. During the experiment, the lateral pressure coefficient decreased as the axial load force increased continuously. In region OA, the lateral pressure coefficient was greater than 1. The axial load-displacement curve of the granite specimen shows deformation characteristics in the compaction stage. In region AB, the lateral pressure coefficient decreased from 1 to 0.148 and the axial load-displacement curve of the granite specimen exhibited elastic deformation characteristics. In region BC, the lateral pressure coefficient decreased from 0.148 to 0.120 and the axial load-displacement curve of the granite specimen showed plastic deformation characteristics.

2.2.2. AE Hit and Energy Distribution Characteristics. The number and total energy of AE hits in each time window were counted over the course of the experiment as shown in Figure 4. Both indicators increased until reaching a peak at about 30 s, then decreased until 100 s. From 100 s to 360 s, they remained basically unchanged. The selection of Point A could be revised at 100 s; the axial force was 15% of the peak stress, 130 kN.

As shown in Figure 4, the number of AE hits increased in a fluctuant manner while the total energy of AE dropped slightly from 560 s to 590 s, which is congruous with the characteristics of the number and total energy of AE hits. The number of AE hits decreased rapidly and the total energy released by AE hits increased rapidly after 590 s. The selection of Point B could be revised accordingly at 590 s; the axial force was 85% of the peak stress, 720 kN.

The region AB can be divided into three phases. In the first phase (from 100 s to 360 s), the number and total energy

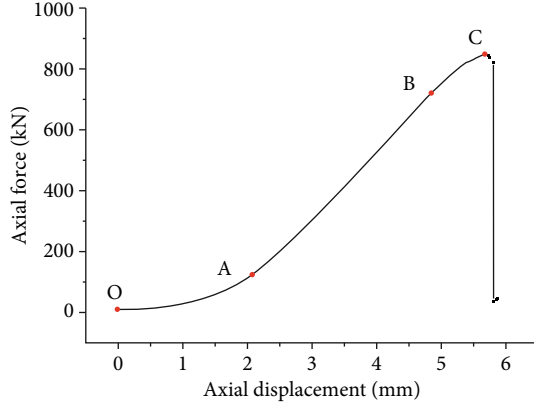


FIGURE 3: Curve of axial force versus axial displacement.

of AE hits was small and relatively constant. In the second phase (from 360 s to 510 s), the number and total energy of AE hits increased in a fluctuant manner. In the third phase (from 510 s to 590 s), the number of AE hits increased in a fluctuant manner while the total energy of AE slightly decreased. The region BC extended from 590 s to 699 s. Gao et al. [42, 43] carried out similar stress-strain curves and generation characteristics of AE, which confirms the repeatability of these experimental results.

Ai et al. (2011) examined the spatial-temporal evolution of AE locations under triaxial compression to find that the number of and energy released by the AE hits first increases and then decreases as axial stress reaches the confining pressure value. This is the so-called “confining pressure effect” of AE. The peak of the number and total energy of AE hits during the OA stage should be also attributed to the confining pressure.

2.3. Evolution Characteristics of High-Energy and Low-Energy AE Hits

2.3.1. Definition of High-Energy and Low-Energy AE Hits

(1) *Average Energy Logarithm Evolution Characteristics of AE Hits.* Ten seconds were selected as a time window and the AEL was calculated to analyze the AE hit energy evolution over the course of the rock specimen failure process. The change curve of AEL versus time during the biaxial compression experiment is shown in Figure 5. This curve can be divided into three stages. In the first stage (from 0 s to 360 s, corresponding to the region OA and the first phase in the region AB), AEL fluctuated around 3.75. In the second stage (from 360 s to 590 s, corresponding to the second and third phases in the region AB), the AEL fluctuated while trending upward. In the third stage (from 590 s to 705 s, corresponding to the region BC), the AEL began to increase rapidly from 4 to 8.23. The average energy corresponding to a given AE hit in the time window increased with some fluctuation after 360 s and significantly increased after 590 s.

(2) *Energy Distribution Evolution Characteristics of AE Hits.* The energy distribution evolution characteristics of AE hits were analyzed as shown in Figure 6. As shown in Figure 7, the density of AE hits versus the logarithm of AE energies obeys a Burr distribution from 0 s to 670 s. However, it did not obey the Burr distribution from 670 s to 705 s. The density function of the Burr distribution can be expressed as follows:

$$f(x | a, c, k) = \frac{(kc/a)(x/a)^{c-1}}{[a + (x/a)^c]^{k+1}}, \quad x > 0, a > 0, c > 0, k > 0, \quad (1)$$

where a is a scale parameter, c is a parameter of inequality, x is the logarithm of energy, and k is a shape parameter.

The peak density as per the AE hit energy distribution increased from $10E2.4$ aJ to $10E3.0$ aJ between 0 s and 670 s. Although the density of AE hits versus the logarithmic AE energies did not obey the Burr distribution from 670 s to 700 s, the peak density increased from $10E3.0$ aJ to $10E5.6$ aJ. The energy of AE hits ranged from $10E1.8$ aJ to $10E5.6$ aJ before 490 s (corresponding to the region OA and the first/second phases in the region AB). After 490 s (corresponding to the third phase in the region AB and the region BC), AE hits with energy larger than $10E5.6$ aJ began to appear, then increased in proportion as the loading time progressed. The AEL evolution characteristics are closely related to the number of AE hits with energy larger than $10E5.6$ aJ.

(3) Evolution Characteristics of Cracks in Granite Specimen.

The evolution of cracks during the biaxial compression experiment is shown in Figure 8. As shown in Figure 8, no obvious microcracks were observed before 477 s. Between 477 s and 587 s, microcracks emerged and developed along the primary structural planes (e.g., interfaces between the groundmass and phenocryst) but did not connect with each other (Figure 6). After 587 s, these microcracks expanded into tensile cracks (PTC), remote cracks (RC), and shear cracks (SC) around the circular opening due to the stress concentration around the opening. The SC continuously expanded and gradually connected with the RC and PTC over the loading time, as similarly observed by Dzik et al. [44], Martin et al. [45], and Zhu et al. [46].

By comparing the energy distribution evolution characteristics of AE hits and the evolution characteristics of cracks, the increase in AE hits with energy $>10E5.6$ aJ was found to be attributable to the evolution and growth of microcracks and cracks in the granite specimen. Thus, AE hits with energy $<10E5.6$ aJ were defined as “low-energy AE hits” and those $>10E5.6$ aJ as “high-energy AE hits.”

2.3.2. Evolution of High-Energy and Low-Energy AE Hits

(1) *Evolution Characteristics of High-Energy and Low-Energy AE Hits.* The energy distribution of AE hits over the course of the experiment is shown in Figure 9(a). The energy of AE hits was mainly distributed in the low-energy range during the experiment. The energy distribution of high-energy AE hits

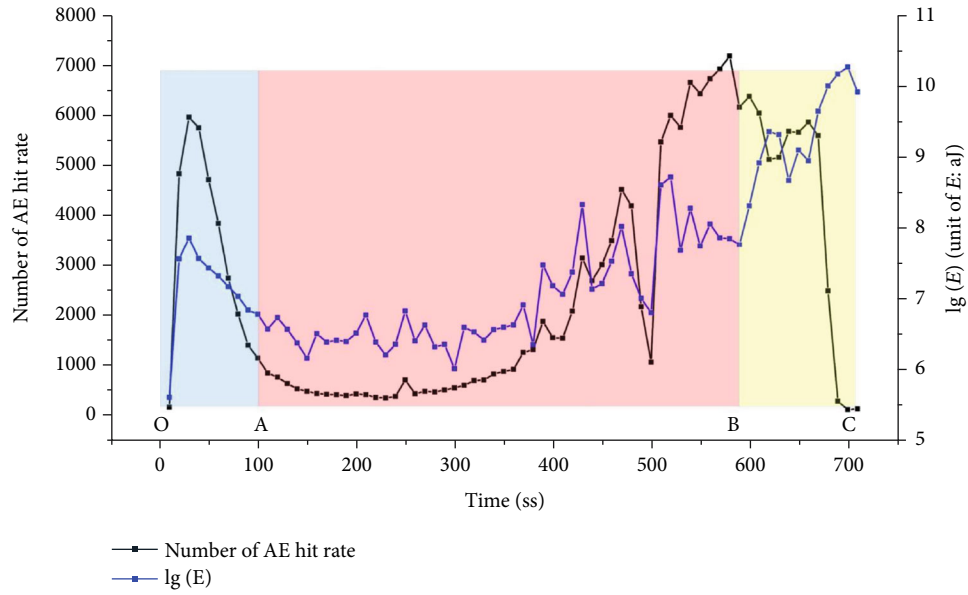


FIGURE 4: Curves of AE hit rate and energy during loading process.

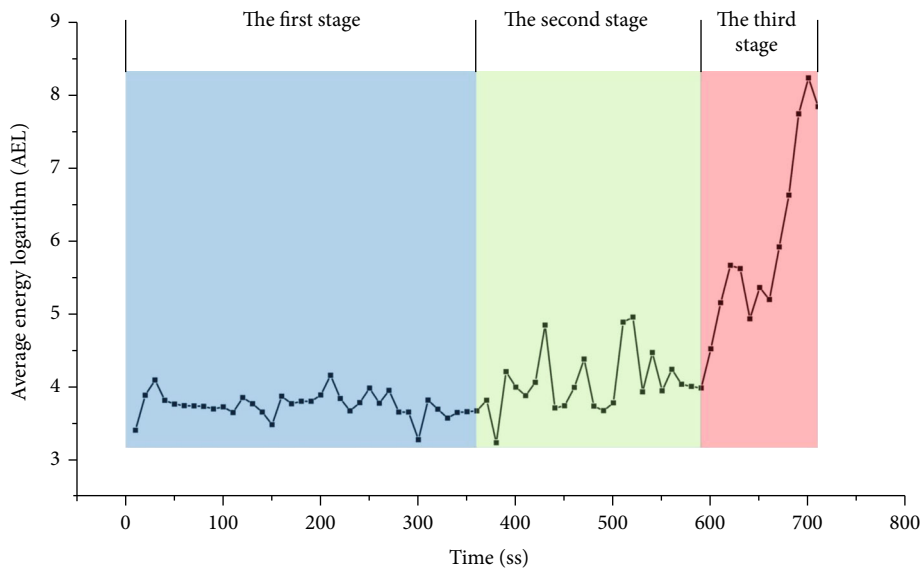


FIGURE 5: Change curve of AEL during the experiment process.

is shown in Figure 9(b). There were fewer high- than low-energy hits, but some did remain in the later stages of the experiment.

AE hits with energy ranging from $10E2.4$ aJ to $10E2.6$ aJ were selected to analyze the low-energy hit evolution characteristics during the experiment; hits ranging from $10E5.8$ aJ to $10E6.0$ aJ were selected to analyze the high-energy hit evolution characteristics during the experiment. As shown in Figure 10(a), the energy evolution characteristics of low-energy AE hits was approximately the same as that of all AE hits. As shown in Figure 8(b), the energy evolution characteristics of high-energy AE hits were quite different from that of low-energy hits and can be divided into three stages: basically negligible in the first loading

stage (before 360 s), increasing slightly in the second loading stage (from 360 s to 490 s), and increasing rapidly in the third loading stage (after 490 s).

The distribution of AE hits and energy monitored during the experiment were mainly dependent on the low-energy AE hits. There also were some similarities among the evolution characteristics of high-energy AE hits and the AEL evolution characteristics of the hits; an increase in the number of the high-energy AE hits is the root cause of an increase in AEL. The evolution characteristics of high-energy AE hits also are in close agreement with the evolution characteristics of cracks in the granite specimen.

(2) *Evolution Mechanism of High-Energy and Low-Energy AE Hits.* The granite specimen used in the experiment has a

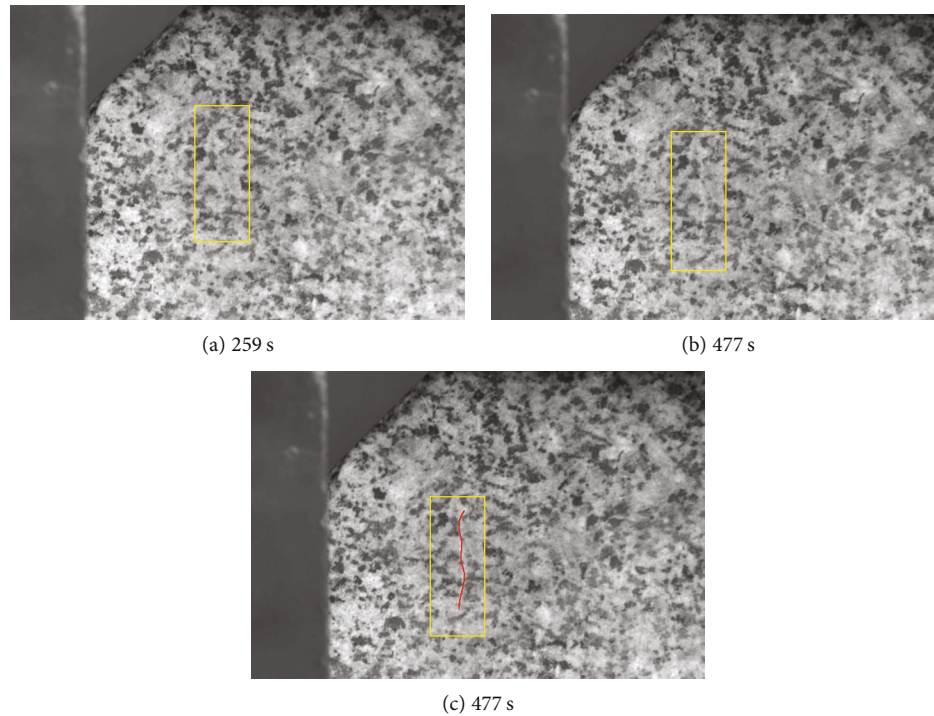


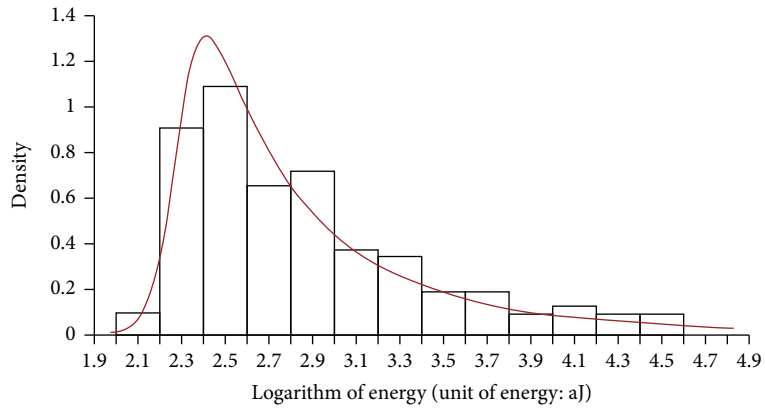
FIGURE 6: Trace of an example microcrack.

porphyritic texture and is composed of two different sizes of granules. Large granules (or “phenocrysts”) were scattered among the small granules (groundmass). The groundmass is composed of microlite, crystallite, cryptocrystalline, or glassy material. In the local region, there were several closely packed, interconnected phenocrysts. Phenocrysts and their interfaces constituted the framework of the granite specimen. The diameter of phenocrysts ranges from 1 mm to 5 mm while that of groundmass granules is less than 1 mm. The evolution mechanism of high-energy and low-energy AE hits can be summarized as per the microscopic structure of the granite specimen, evolution characteristics of cracks in the granite specimen, and the evolution mechanism of high-energy and low-energy AE hits.

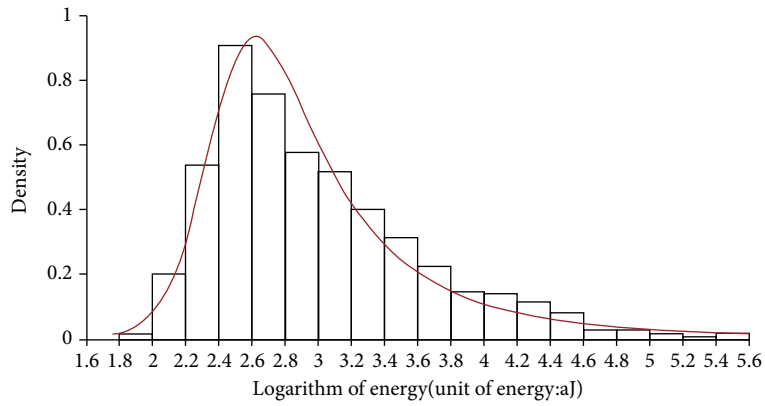
In the early stage of the loading process (before 490 s, corresponding to the region OA and the first/second phases in the region AB), low-energy AE hits caused by failure of the small groundmass occurred in the granite specimen. Though groundmass failure had little effect on the damage of the granite specimen, it led to the stress concentration in the specimen’s framework (which did not fail in this stage). As the loading increased, the interfaces of one phenocryst to another phenocryst or to the groundmass failed and produced high-energy AE events. The granite specimen entered the midstage of the loading process at this point (from 490 s to 590 s, corresponding to the third phase in the region AB), where the number of low-energy AE hits was much higher than that of high-energy AE hits.

As the number of the failed interfaces continued to increase, stress transferred to the phenocrysts in the granite specimen and caused them to fail alongside the emergence of high-energy AE events. Failure of both the interfaces and phenocrysts damaged the granite specimen. Once a certain amount of damage had accumulated, the granite specimen entered the later stage of the loading process (from 590 s to 705 s, corresponding to the region BC). Phenocrysts inside the specimen failed and quickly penetrated the primary structural planes, which ultimately led to the failure and instability of the whole specimen. A rapid increase in the number of high-energy AE hits (with still relatively few low-energy hits) is an important indicator that this stage has begun. The evolution mechanism of high energy and low energy AE hits explains this phenomenon that the closer to failure AE data are used as initial input into the AE data-driven model to simulate the rock failure process, the better the model predictions of failure are by Wei et al. [47].

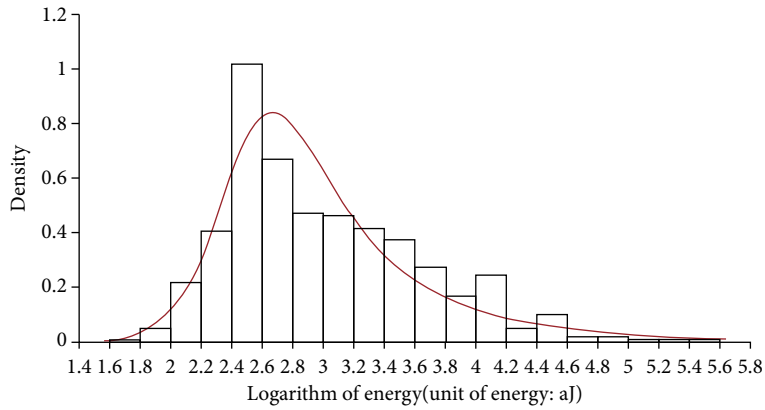
(3) *Relationship between Evolution Mechanism and Gutenberg-Richter b Value.* The Gutenberg-Richter b value was calculated over the loading process. Ten seconds was selected as a time window representative of the whole biaxial compression experiment. The b value in each time window was calculated to determine its variations with time as shown in Figure 11. The b value fluctuated around 0.83 before 490 s (corresponding to the region OA and the first/second phases in the region AB) and decreased slightly from 490 s to 590 s (corresponding to the third phase in the region AB), then



(a) Density of AE hits (from 0 s to 10 s)



(b) Density of AE hits (from 100 s to 110 s)



(c) Density of AE hits (from 280 s to 290 s)

FIGURE 7: Continued.

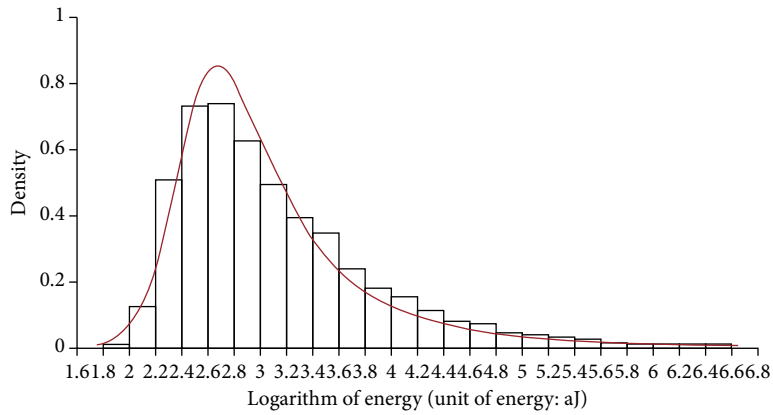
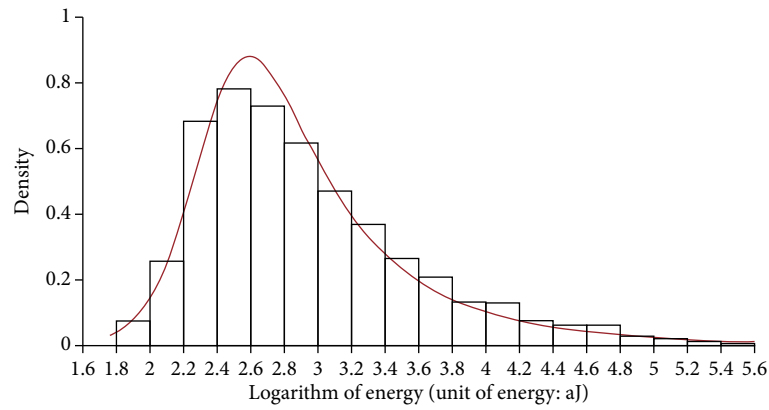
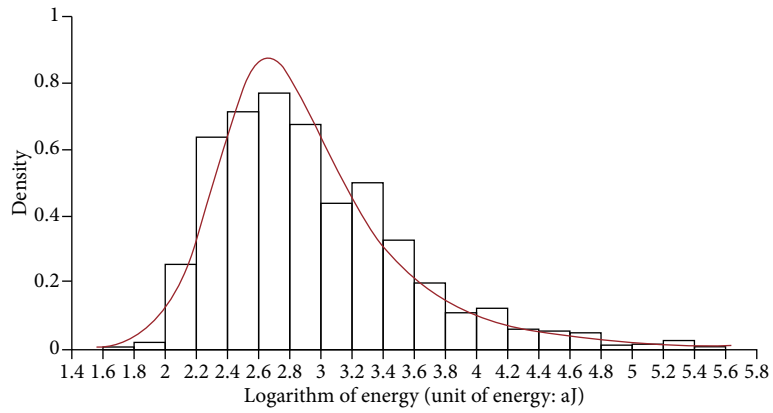
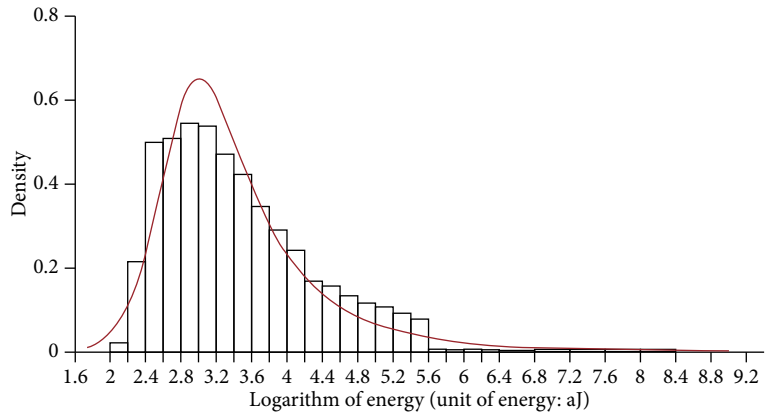
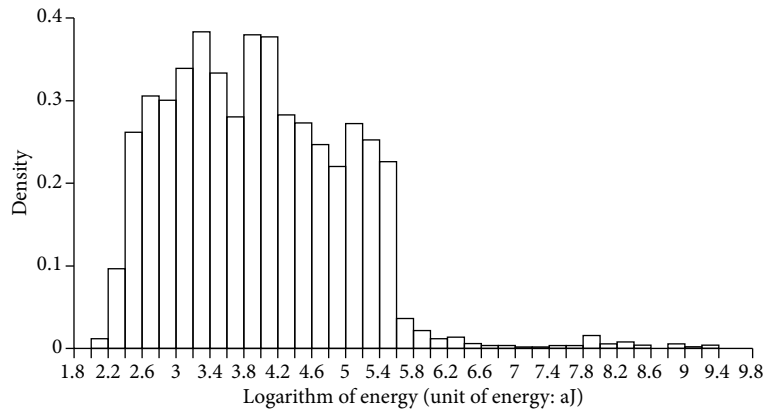


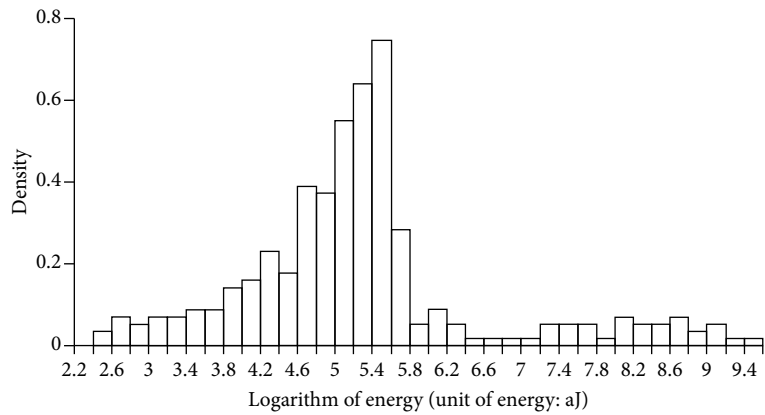
FIGURE 7: Continued.



(g) Density of AE hits (from 660 s to 670 s)

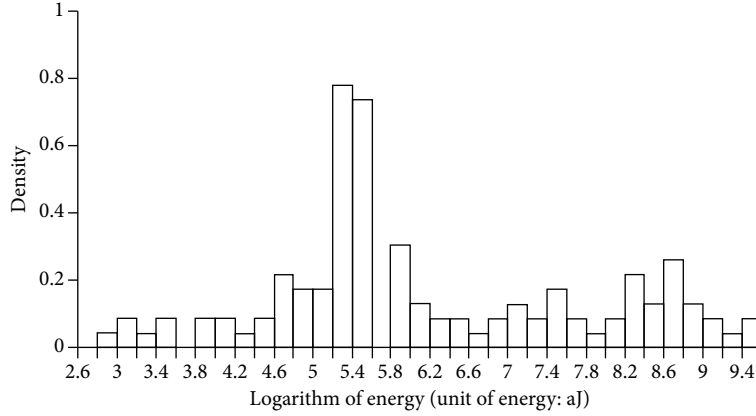


(h) Density of AE hits (from 670 s to 680 s)



(i) Density of AE hits (from 680 s to 690 s)

FIGURE 7: Continued.



(j) Density of AE hits (from 690 s to 700 s)

FIGURE 7: Energy distribution of AE hits (note: the red curve is the fitting result with the Burr distribution model).

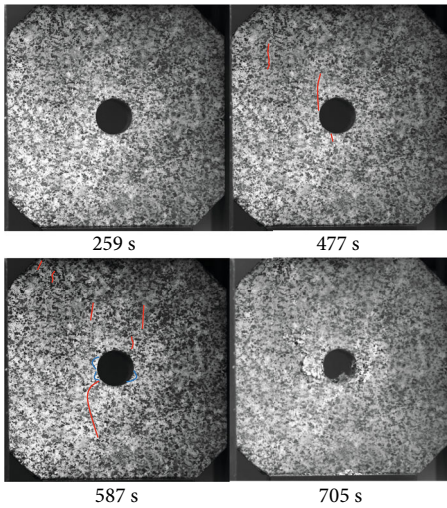


FIGURE 8: Crack evolution characteristics during biaxial compression experiment (note: microcracks marked with red lines, macrocracks marked with blue lines).

declined rapidly after 590 s (corresponding to the region BC). At 490 s, the axial loading force increased to 72% of the peak loading value. At 590 s, the axial loading force increased to 85% of the peak loading value (corresponding to Point C in the axial load-displacement curve).

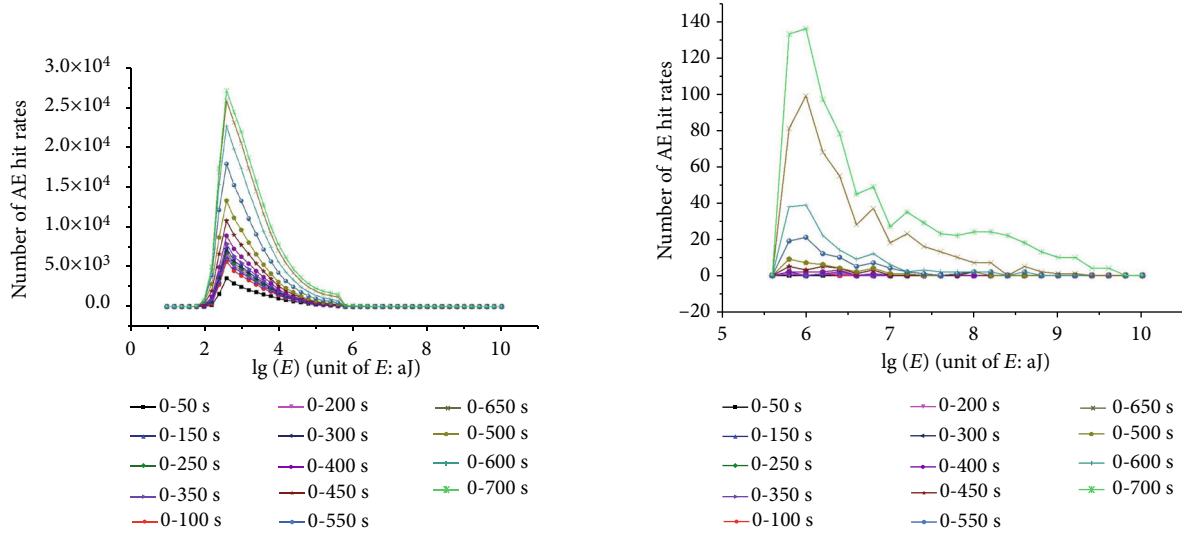
The high-energy AE hit evolution characteristics were inversely proportional to the Gutenberg-Richter b value of the granite specimen during the loading process. The increase in low-energy AE hits did not cause the Gutenberg-Richter b value to change, but the increase in high-energy hits caused the Gutenberg-Richter b value to decrease. A larger b value decreasing rate created a larger increasing high-energy AE hit rate. This further validates the high- and low-energy AE hit evolution mechanism presented above.

3. High-Energy and Low-Energy MS Event Evolution Characteristics

3.1. Engineering Geology and MS Monitoring System. General geological information for the Dongjiahe Coal Mine and MS monitoring system used in this study is given in a previous publication by Cheng et al. [15]. Briefly, the Dongjiahe Coal Mine is located in northwestern China. The No. 22517 working face is a typical advancing mining face which has a length of 1217 m, width of 185 m, and dips from east to west. The inclination angle of the working face is approximately 3° , making it nearly horizontal. The open cut is located at 1217 m and the mining stop line at 100 m. The coal seam in the working face varies in thickness from 2.5 m to 4.1 m with an average thickness of 3.3 m. The schematic sketch of the No. 22517 working face is shown in Figure 12. The advancement schedule of the No. 22517 working face is given in Table 1.

According to the drill histogram of No. 22517 (Figure 13), the rock mass strata around the working face is, according to the ages of formation from old to new, as follows: middle Ordovician System, Fengfeng Formation; upper Carboniferous System, Taiyuan Formation; lower Permian System, Shanxi Formation; lower Permian System, Xiashihezi Formation; and Quaternary System overburden soil.

Geophones with 43.3 V/m/s sensitivity were adopted in the MS monitoring system used in this study. The response frequency of geophones ranges from 15 to 1000 Hz. The geophone placement scheme for MS monitoring is given in detail by Cheng et al. [15]. The Geiger location method was used here to localize the MS. The P-wave velocity was estimated at 2800 m/s and the S-wave velocity at 1800 m/s based on artificial blasting tests. The ESG microseismic monitoring system is used for signal acquisition, including Paladin underground digital signal acquisition system, Hyperion surface digital signal processing system, and MMVTS-3D visualization software. The system can monitor continuously 24 hours in real time. Many focal parameters such as time-



(a) Energy distribution of all AE hits during the experiment process (b) Energy distribution of high-energy AE hits during the experiment process

FIGURE 9: Energy distribution of AE hits during the experiment process.

space coordinates, errors, magnitude, and energy of microseismic events can be obtained. The collected data can be filtered, and the complete waveform and spectrum analysis chart of source information can be provided. At the same time, it can automatically identify the type of microseismic events and eliminate noise events by filtering, threshold setting and bandwidth detection.

3.2. Evolution Characteristics of High-Energy and Low-Energy MS Events. Basic MS monitoring results are given in the previous publication by Cheng et al. [15]. The energy and moment magnitude of MS events over coal seams caused by mining activities were analyzed based on this information; the results are shown in Figure 14. As shown in Figures 14(a) and 14(b), the energy distribution and the moment magnitude distribution of MS events conformed in this case to the BMD. The energy of low-energy MS events was less than 158.5 J, while the energy of high-energy MS events was greater than 158.5 J (Figure 14(a)). The moment of low-energy MS events was less than -0.1, while the energy of high-energy MS events was greater than -0.1 (Figure 14(b)).

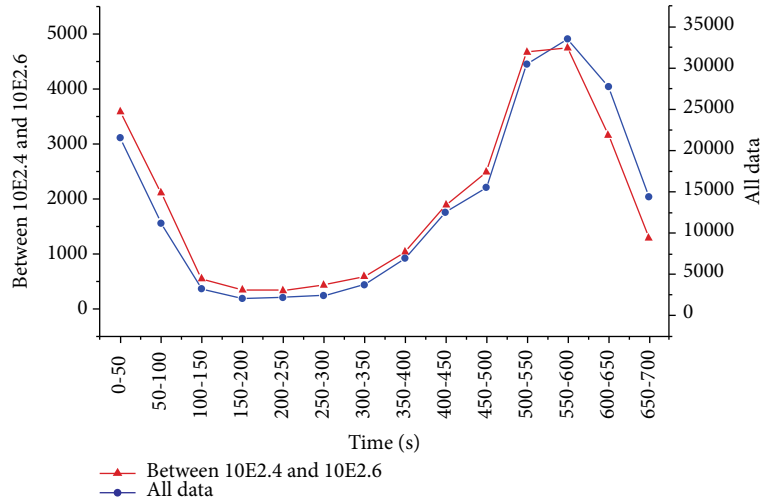
The average energy logarithm (AEL) was defined to further analyze the difference between high- and low-energy MS event components. The AEL is a logarithm of the ratio of the total energy to the number of all MS events in a one-day period (Formula (2)). Its physical meaning corresponds to the average energy of MS events in a given day. The curve of AEL versus time is given in Figure 14(c), where AEL mainly varied between 0.5 and 2.0 from Nov. 25, 2014, to Feb. 25, 2015, and between 2.8 and 4.1 from Feb. 25, 2015, to Oct. 10, 2015. The high-energy MS event components appear to have increased rapidly after Feb. 25.

$$AEL = \lg (E_w / N_w), \quad (2)$$

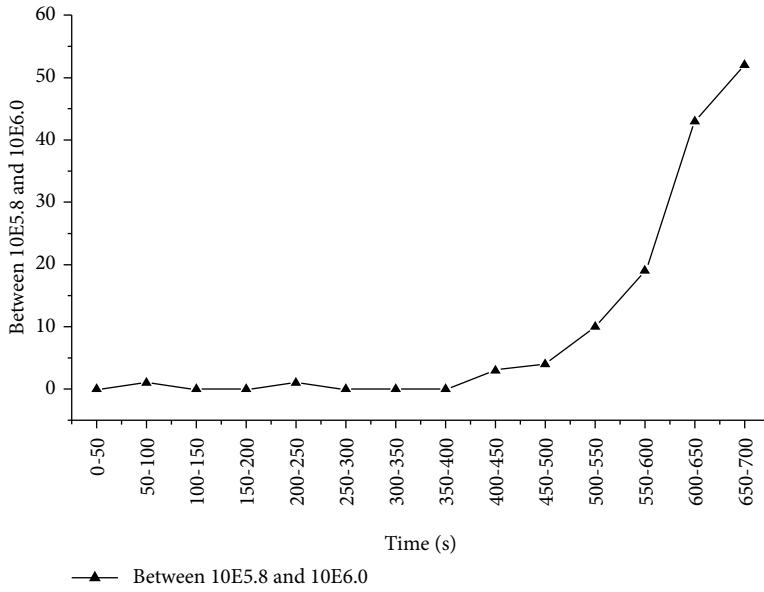
where AEL is the average energy logarithm, N_w is the number of MS events in a day, and E_w is the sum of energy of MS events in a day.

Cheng et al. [15] introduced time-, location-, and energy-related evolution characteristics of MS events in the roof of the Dongjiahe Coal Mine. Based on their monitoring results, new MS events added monthly fell into the region from 30 m behind the mining face to 220 m in front of the mining face along the horizontal direction and in the region from the elevation of +320 m to +500 m along the vertical direction after Mar. 6, 2015 [15]. Most of the new MS events added monthly were concentrated in the coal pillar supporting zone, the support and bed-separation zone along the horizontal direction, and from the top of the fractured zone to the bottom of the continuous zone along the vertical direction. Based on the conceptual model proposed by Qian et al. [48], the rock mass was in a state of near failure or had already failed in the zone where these new monthly MS events occurred. By Feb. 25, 2015, the working face had advanced 360 m (about twice the width of the working face) from the open cut to the stopping line.

The MS monitoring data suggests that the working face was in the insufficient mining stage (in the stage, only the collapse zone is formed but the fracture zone is not formed in the process of rock failure; the maximum subsidence value of the strata continues to increase) before Feb. 25 and that the height of the fracture zone caused by mining did not develop to the final height. After Feb. 25, the working face was in the sufficient mining stage (in this stage, the size of the goaf is large enough and the maximum subsidence value of the strata does not increase) and the fracture zone developed to the final height. Thus, the high-energy MS events occurred beginning on Feb. 25, because the failure scale of the overlying rock mass increased upon the working face entering the sufficient mining stage.



(a) Energy evolution characteristics of low-energy AE hits



(b) Energy evolution characteristics of high-energy AE hits

FIGURE 10: Energy evolution characteristics of low-energy and high-energy AE hits.

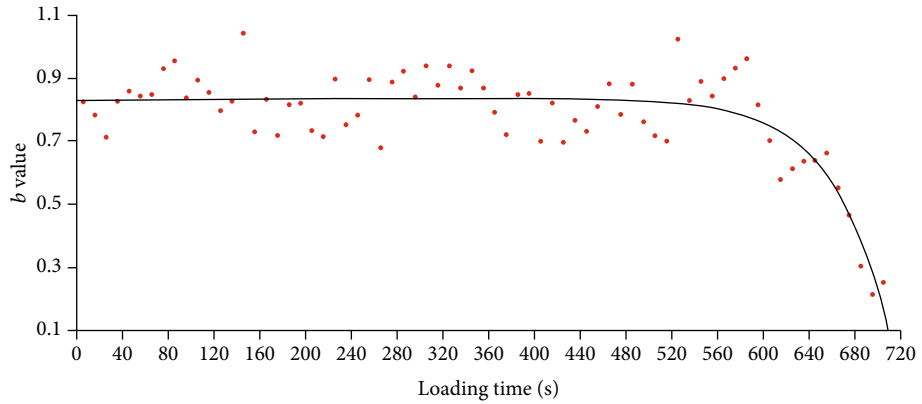


FIGURE 11: Change of b value of Gutenberg-Richter during loading process.

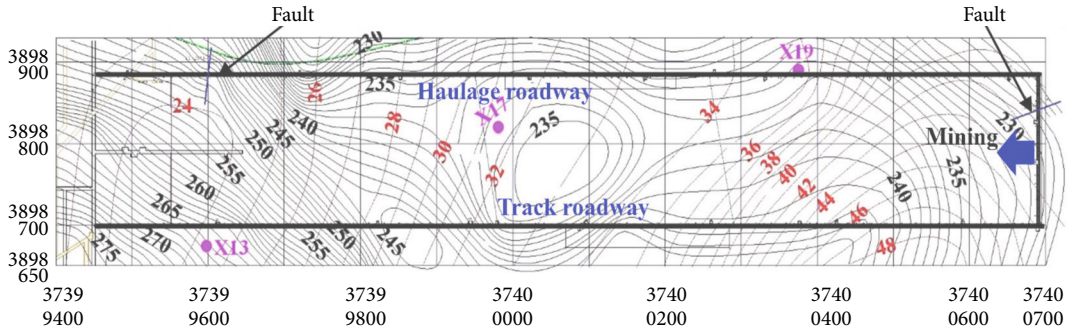


FIGURE 12: Schematic sketch of coal seam of No. 22517 working face.

TABLE 1: Mining schedule, No. 22517 working face of Dongjiahe Coal Mine [15].

Date (year/month/day)	The mining face (pitch distance)
2014/12/23	1005 m
2015/01/09	981 m
2015/01/19	942 m
2015/01/30	917 m
2015/02/09	885 m
2015/02/15	856 m
2015/02/27	847 m
2015/03/09	803 m
2015/03/19	779 m
2015/03/30	760 m
2015/04/09	714 m
2015/04/18	700 m
2015/04/29	694 m
2015/05/08	688 m
2015/05/19	681 m
2015/05/30	750 m
2015/06/09	745 m
2015/06/19	736 m
2015/06/29	730 m
2015/07/09	720 m
2015/07/18	677 m
2015/07/30	665 m
2015/08/08	657 m
2015/08/15	648 m
2015/08/19	642 m
2015/08/30	628 m
2015/09/08	615 m
2015/09/19	603 m
2015/09/29	592 m
2015/10/09	578 m

4. Discussion

There are some similarities among the evolution characteristics of high-energy MS events and low-energy AE hits. Both

have bimodal characteristics and can be divided into the high-energy and low-energy components. An increase in the failure scale is the root cause of an increase in the high-energy component. There is also a significant difference between the two: the bimodal distribution of AE hits is far less obvious than that of MS events. There are two potential reasons for this.

The first reason involves differences in the monitoring equipment. The frequency range of the R6a sensor in the AE monitoring system extends from 35 kHz to 100 kHz while that of the geophone in the MS monitoring system is from 15 Hz to 1000 Hz. The bandwidth of the AE monitoring system is much larger than that of the MS monitoring system. In addition, the scale of the AE monitoring system monitoring object is far smaller than that of the MS monitoring system monitoring object. Therefore, the AE monitoring system serves to detect AE events caused by the full-scale microcracks of rock specimens during the experiment while the MS monitoring system cannot detect the MS events caused by small-scale microcracks, which are the main components of low-energy MS events.

The second reason involves differences in the monitoring object. In this study, the object of the AE monitoring system is a granite specimen while that of the MS monitoring system is sandstone/mudstone. Granite is an igneous rock; sandstone and mudstone are sedimentary. The diagenesis of igneous rock material differs from that of sedimentary rock materials, so there are substantial differences between the microstructures of granite and sandstone and mudstone. The rock specimen used in the laboratory was not designed with consideration of its structural plane, though the in situ rock mass contains a large number of original structural planes. These factors may have made the BMD of AE hits less obvious than that of MS events.

5. Conclusions

Microseismic and acoustic emission monitoring are always carried out in engineering rock masses and experimental rocks, and the evolution characteristics of high-energy and low-energy events occurring in the deformation of the rock are instructive for optimizing monitoring and understanding the failure mechanism. In this study, combining the granite specimen biaxial compression experiment and the MS monitoring results of the 22517 working face in the Dongjiahe

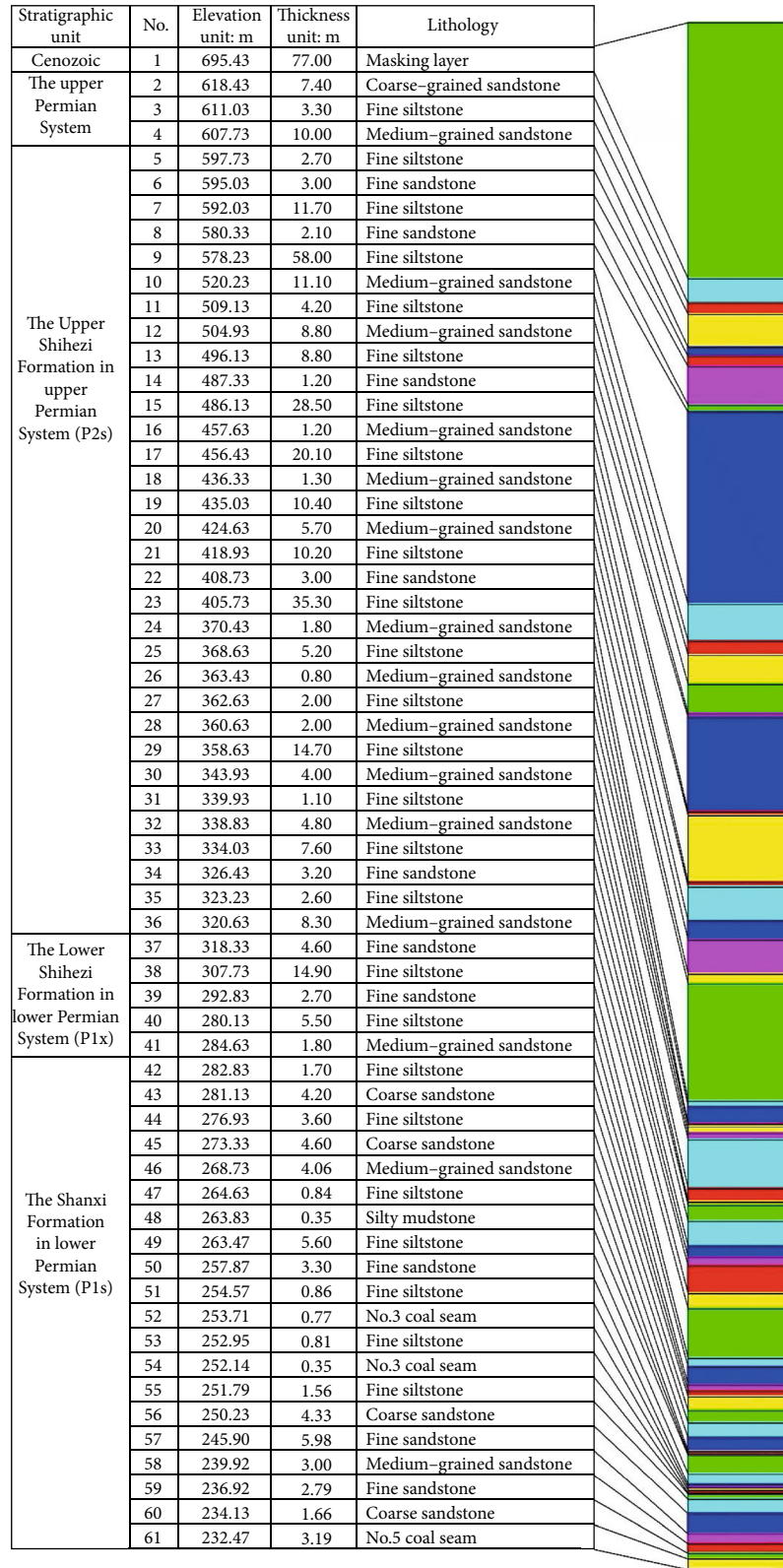
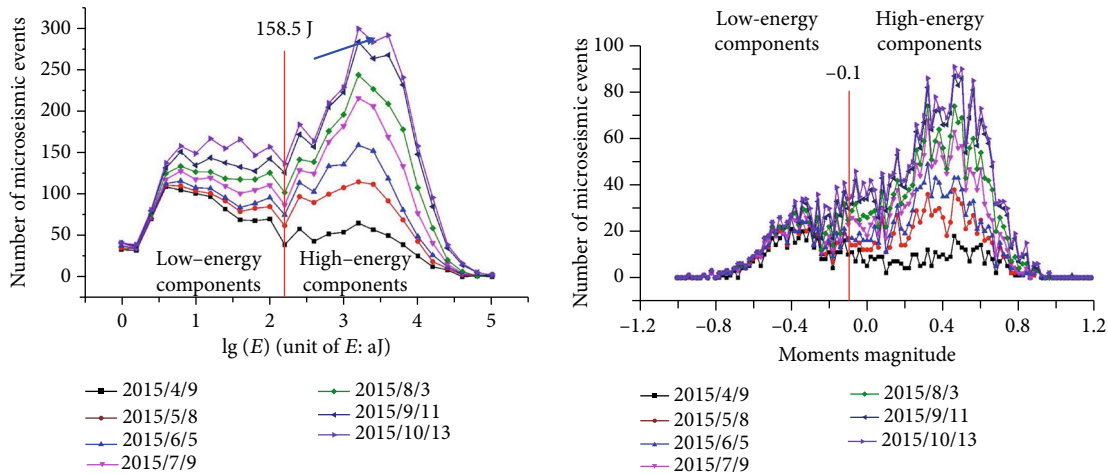


FIGURE 13: Drill histogram of No. 22517 working face [15].

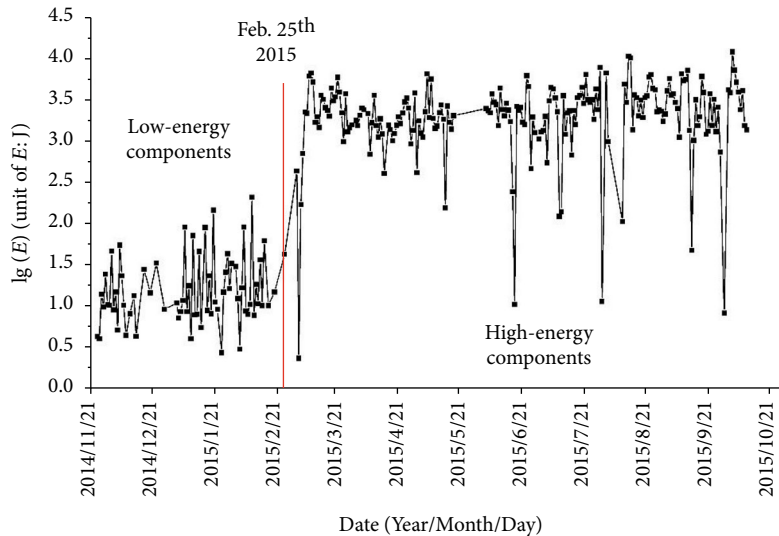
Coal Mine, the evolution characteristics of microseismic events were analyzed based on the bimodal distribution (BMD) model, and the following conclusions were obtained:

- (1) The MS monitoring results of No. 22517 working face in Dongjiahe Coal Mine show unimodal energy and moment magnitude distributions from Nov. 25,



(a) Energy distribution characteristic of microseismic events in No. 22517 working face

(b) Moment magnitude distribution characteristic of microseismic events in No. 22517 working face



(c) Curve of energy index with time in No. 22517 working face

FIGURE 14: Energy and moment magnitude distribution of MS events.

2014, to Feb. 25, 2015; the distributions were bimodal from Feb. 25, 2015, to Oct. 10, 2015. High-energy MS events were generated due to an increase in the failure scale of the overlying rock mass once the working face crossed into the sufficient mining stage from the insufficient mining stage

(2) Biaxial compression experiments were conducted on a granite specimen to observe various characteristics of low- and high-energy AE hits. The whole loading process was divided into three stages. In the first loading stage, only low-energy AE hits occurred. In the second loading stage, high-energy AE hits began to appear and slowly grew more common. In the third loading stage, the quantity of high-energy AE hits increased rapidly until the specimen failed. Low-energy AE hits were more common than high-energy AE hits throughout the whole loading process, but the change characteristics

of the high-energy hits appeared to be positively correlated with the evolution of cracks in the granite specimen and negatively correlated with changes in the Gutenberg-Richter b value. The high-energy and low-energy AE hit evolution mechanism was defined here based on the microscopic structure of the granite specimen

(3) This paper discussed the similarities and differences between the evolution of high-energy MS events and low-energy AE hits. Both were found to have bimodal characteristics and can be divided into high-energy and low-energy components. An increase in the failure scale is the root cause of the increase observed in the high-energy component. The bimodal distribution of AE hits was far less obvious than that of MS events, which is likely attributable to differences in the monitoring equipment and monitoring object

Data Availability

As for the data availability statement, some or all data, models, or code generated or used during the study are available from the corresponding author by request (list items).

Conflicts of Interest

No conflict of interest exists in the submission of this manuscript.

Authors' Contributions

The manuscript is approved by all authors for publication.

Acknowledgments

We thank Shaanxi Coal and Chemical Technology Institute Co., Ltd. for approving our publication, and the personnel at the Dongjiahe coal mine. We thank Dalian University of Technology for facilitating our project and personnel at the State Key Laboratory of Coastal and Offshore Engineering in Dalian University of Technology. The project was funded by the National Science Foundation of China (Grant Nos. 51909032, 51627804, and U1710253) and Department of Science and Technology of Anhui Province (Nos. 2008085ME145 and 17030901023).

References

- [1] S. Gibowicz and A. Kijko, *An Introduction to Mining Seismology*, Elsevier, 1994.
- [2] A. Kijko, M. Dessokey, E. Głowacka, and M. Kazimierczyk, "Periodicity of strong mining tremors in the Lubin copper mine," *Acta Geophysica Polonica*, vol. 30, pp. 221–230, 1982.
- [3] I. Main, "A characteristic earthquake model of the seismicity preceding the eruption of Mount St. Helens on 18 May 1980," *Physics of the Earth and Planetary Interiors*, vol. 49, no. 3–4, pp. 283–293, 1987.
- [4] I. Main and P. Burton, "Physical links between crustal deformation, seismic moment and seismic hazard for regions of varying seismicity," *Geophysical Journal International*, vol. 79, no. 2, pp. 469–488, 1984.
- [5] T. Stankiewicz, *Stochastic Model of Seismic Activity and its Application to Seismic Hazard Estimates in Mines*, Institute of Geophysics, Polish Academy of Sciences, Warsaw, 1989.
- [6] A. Kijko, B. Drzezla, and T. Stankiewicz, "Bimodal character of the distribution of extreme seismic events in Polish mines," *Acta Geophysica Polonica*, vol. 35, no. 2, pp. 157–166, 1988.
- [7] T. Li, T. Mei, X. Sun, Y. Lv, J. Sheng, and M. Cai, "A study on a water-inrush incident at Laohutai coalmine," *International Journal of Rock Mechanics and Mining Sciences*, vol. 59, pp. 151–159, 2013.
- [8] K. Zhang, T. Yang, H. Bai, and R. Pathagama Gamage, "Long-wall mining-induced damage and fractures: field measurements and simulation using FDM and DEM coupled method," *International Journal of Geomechanics*, vol. 18, no. 1, article 04017127, 2018.
- [9] Y. Xiao, X. T. Feng, J. A. Hudson, B. R. Chen, G. L. Feng, and J. P. Liu, "ISRM suggested method for in situ microseismic monitoring of the fracturing process in rock masses," *Rock Mechanics and Rock Engineering*, vol. 49, no. 1, pp. 343–369, 2016.
- [10] G. Feng, X. Feng, B. Chen, Y. X. Xiao, and Y. Yu, "A microseismic method for dynamic warning of rockburst development processes in tunnels," *Rock Mechanics and Rock Engineering*, vol. 48, no. 5, pp. 2061–2076, 2015.
- [11] N. Xu, T. Li, F. Dai, R. Zhang, C. A. Tang, and L. X. Tang, "Microseismic monitoring of strainburst activities in deep tunnels at the Jinping II hydropower station, China," *Rock Mechanics and Rock Engineering*, vol. 49, no. 3, pp. 981–1000, 2016.
- [12] Y. Yu, B. Chen, C. Xu, X. H. Diao, Tong, and Y. F. Shi, "Analysis for microseismic energy of immediate rockbursts in deep tunnels with different excavation methods," *International Journal of Geomechanics*, vol. 17, no. 5, article 04016119, 2017.
- [13] Y. Yu, D. Geng, L. Tong, X. S. Zhao, X. H. Diao, and L. H. Huang, "Time fractal behavior of microseismic events for different intensities of immediate rock bursts," *International Journal of Geomechanics*, vol. 18, no. 7, article 06018016, 2018.
- [14] J. Wang, J. Liu, H. Liu, Z. Tian, and F. Cheng, "Modeling and locating underground water pipe leak with microseismic data," *Journal of Applied Geophysics*, vol. 136, pp. 1–8, 2017.
- [15] G. Cheng, T. Ma, C. Tang, H. Liu, and S. Wang, "A zoning model for coal mining-induced strata movement based on microseismic monitoring," *International Journal of Rock Mechanics and Mining Sciences*, vol. 94, pp. 123–138, 2017.
- [16] A. Cao, L. Dou, W. Cai, S. Gong, S. Liu, and G. Jing, "Case study of seismic hazard assessment in underground coal mining using passive tomography," *International Journal of Rock Mechanics and Mining Sciences*, vol. 78, pp. 1–9, 2015.
- [17] A. Cao, L. Dou, C. Wang, X. X. Yao, J. Y. Dong, and Y. Gu, "Microseismic precursory characteristics of rock burst hazard in mining areas near a large residual coal pillar: a case study from Xuzhuang coal mine, Xuzhou, China," *Rock Mechanics and Rock Engineering*, vol. 49, no. 11, pp. 4407–4422, 2016.
- [18] D. Li, Q. Zhu, Z. Zhou, X. Li, and P. G. Ranjith, "Fracture analysis of marble specimens with a hole under uniaxial compression by digital image correlation," *Engineering Fracture Mechanics*, vol. 183, pp. 109–124, 2017.
- [19] C. Lu, L.-M. Dou, H. Liu, H.-S. Liu, B. Liu, and B.-B. Du, "Case study on microseismic effect of coal and gas outburst process," *International Journal of Rock Mechanics & Mining Sciences*, vol. 53, pp. 101–110, 2012.
- [20] T. Li, M. Cai, and M. Cai, "Earthquake-induced unusual gas emission in coalmines-A km-scale in-situ experimental investigation at Laohutai mine," *International Journal of Coal Geology*, vol. 71, no. 2–3, pp. 209–224, 2007.
- [21] P. Zhang, T. Yang, Q. Yu, T. Xu, W. Shi, and S. Li, "Study of a seepage channel formation using the combination of microseismic monitoring technique and numerical method in Zhangmatun Iron Mine," *Rock Mechanics & Rock Engineering*, vol. 49, no. 9, pp. 3699–3708, 2016.
- [22] N. Xu, C. A. Tang, L. C. Li et al., "Microseismic monitoring and stability analysis of the left bank slope in Jinping first stage hydropower station in southwestern China," *International Journal of Rock Mechanics and Mining Sciences*, vol. 48, no. 6, pp. 950–963, 2011.
- [23] F. Dai, B. Li, N. Xu, G. Meng, J. Wu, and Y. Fan, "Microseismic monitoring of the left bank slope at the Baihetan Hydropower Station, China," *Rock Mechanics and Rock Engineering*, vol. 50, no. 1, pp. 225–232, 2017.

- [24] M. Salvoni and P. Dight, "Rock damage assessment in a large unstable slope from microseismic monitoring-MMG Century mine (Queensland, Australia) case study," *Engineering Geology*, vol. 210, pp. 45–56, 2016.
- [25] H. Alkan, Y. Cinar, and G. Pusch, "Rock salt dilatancy boundary from combined acoustic emission and triaxial compression tests," *International Journal of Rock Mechanics & Mining Sciences*, vol. 44, no. 1, pp. 108–119, 2007.
- [26] S. Hall, F. Sanctis, and G. Viggiani, "Monitoring fracture propagation in a soft rock (Neapolitan tuff) using acoustic emissions and digital images," *Pure and Applied Geophysics*, vol. 163, no. 10, pp. 2171–2204, 2006.
- [27] X. Zhao, J. Wang, M. Cai et al., "Influence of unloading rate on the strainburst characteristics of Beishan granite under true-triaxial unloading conditions," *Rock Mechanics and Rock Engineering*, vol. 47, no. 2, pp. 467–483, 2014.
- [28] M. He, J. Miao, and J. Feng, "Rock burst process of limestone and its acoustic emission characteristics under true-triaxial unloading conditions," *International Journal of Rock Mechanics and Mining Sciences*, vol. 47, no. 2, pp. 286–298, 2010.
- [29] H. Ji, H. Wang, S. Cao, Z. Hou, and Y. Jin, "Experimental research on frequency characteristics of acoustic emission signals under uniaxial compression of granite," *Chinese Journal of Rock Mechanics and Engineering*, vol. 31, no. 1, pp. 2900–2905, 2012.
- [30] P. Benson, B. Thompson, P. G. Meredith, S. Vinciguerra, and R. P. Young, "Imaging slow failure in triaxially deformed Etna basalt using 3D acoustic-emission location and X-ray computed tomography," *Geophysical Research Letters*, vol. 34, no. 3, article L03303, 2007.
- [31] J. Fortin, S. Stanchits, G. Dresen, and Y. Gueguen, "Acoustic emissions monitoring during inelastic deformation of porous sandstone: comparison of three modes of deformation," *Pure and Applied Geophysics*, vol. 166, no. 5-7, pp. 823–841, 2009.
- [32] S. Yang, H. Jing, and S. Wang, "Experimental investigation on the strength, deformability, failure behavior and acoustic emission locations of red sandstone under triaxial compression," *Rock Mechanics and Rock Engineering*, vol. 45, no. 4, pp. 583–606, 2012.
- [33] Y. Li, J. P. Liu, X. D. Zhao, and Y. J. Yang, "Experimental studies of the change of spatial correlation length of acoustic emission events during rock fracture process," *International Journal of Rock Mechanics and Mining Sciences*, vol. 47, no. 8, pp. 1254–1262, 2010.
- [34] H. Xie, J. F. Liu, Y. Ju, J. Li, and L. Z. Xie, "Fractal property of spatial distribution of acoustic emissions during the failure process of bedded rock salt," *International Journal of Rock Mechanics and Mining Sciences*, vol. 48, no. 8, pp. 1344–1351, 2011.
- [35] R. Zhang, F. Dai, M. Gao, N. W. Xu, and C. P. Zhang, "Fractal analysis of acoustic emission during uniaxial and triaxial loading of rock," *International Journal of Rock Mechanics & Mining Sciences*, vol. 79, pp. 241–249, 2015.
- [36] S. Chang and C. Lee, "Estimation of cracking and damage mechanisms in rock under triaxial compression by moment tensor analysis of acoustic emission," *International Journal of Rock Mechanics & Mining Sciences*, vol. 41, no. 7, pp. 1069–1086, 2004.
- [37] N. Dixon and M. Spriggs, "Quantification of slope displacement rates using acoustic emission monitoring," *Canadian Geotechnical Journal*, vol. 44, no. 8, pp. 966–976, 2007.
- [38] N. Dixon, M. P. Spriggs, A. Smith, P. Meldrum, and E. Haslam, "Quantification of reactivated landslide behaviour using acoustic emission monitoring," *Landslides*, vol. 12, no. 3, pp. 549–560, 2015.
- [39] A. Smith, N. Dixon, R. Moore, and P. Meldrum, "Photographic feature: acoustic emission monitoring of coastal slopes in NE England, UK," *Quarterly Journal of Engineering Geology and Hydrogeology*, vol. 50, no. 3, pp. 239–244, 2017.
- [40] A. Smith, N. Dixon, and G. Fowmes, "Early detection of first-time slope failures using acoustic emission measurements: large-scale physical modelling," *Géotechnique*, vol. 67, no. 2, pp. 138–152, 2017.
- [41] Z. Zhong, R. Deng, L. Lv, X. Fu, and J. Yu, "Fracture mechanism of naturally cracked rock around an inverted U-shaped opening in a biaxial compression test," *International Journal of Rock Mechanics and Mining Sciences*, vol. 103, pp. 242–253, 2018.
- [42] X. Gao, S. Liu, and J. Huang, "Acoustic emission characteristics of different areas in the fracture process of perforated granite," *Journal of Northeastern University*, vol. 39, no. 11, pp. 136–140, 2018.
- [43] X. Gao, S. Liu, J. Huang, Z. Yang, W. Mao, and L. Wu, "The influence of strain rate on AE characteristics during rock deformation," *Chinese Journal of Rock Mechanics and Engineering*, vol. 37, no. 4, pp. 887–897, 2018.
- [44] E. Dzik and E. Lajtai, "Primary fracture propagation from circular cavities loaded in compression," *International Journal of Fracture*, vol. 79, no. 1, pp. 49–64, 1996.
- [45] C. Martini, R. Read, and J. Martino, "Observations of brittle failure around a circular test tunnel," *International Journal of Rock Mechanics and Mining Sciences and Geomechanics Abstracts*, vol. 34, no. 7, pp. 1065–1073, 1997.
- [46] W. Zhu, J. Liu, C. Tang, X. D. Zhao, and B. H. Brady, "Simulation of progressive fracturing processes around underground excavations under biaxial compression," *Tunnelling and Underground Space Technology*, vol. 20, no. 3, pp. 231–247, 2005.
- [47] J. Wei, W. Zhu, K. Guan, J. Zhou, and J. J. Song, "An acoustic emission data-driven model to simulate rock failure process," *Rock Mechanics and Rock Engineering*, vol. 53, no. 4, pp. 1605–1621, 2020.
- [48] M. Qian and H. Li, "The movement of overlying strata in long-wall mining and its effect on ground pressure," *Journal of China Coal Society*, vol. 2, pp. 1–12, 1982.